Observation of nonlinearity and heating-induced frequency shifts in cavity magnonics

Wei-Jiang Wu(吴维江), Da Xu(徐达)†, Jie Qian(钱洁), Jie Li(李杰), Yi-Pu Wang(王逸璞)‡, and Jian-Qiang You(游建强)

Interdisciplinary Center of Quantum Information and Zhejiang Province Key Laboratory of Quantum Technology and Device, Department of Physics and State Key Laboratory of Modern Optical Instrumentation, Zhejiang University, Hangzhou 310027, *China*

(Received 8 June 2022; revised manuscript received 16 September 2022; accepted manuscript online 18 October 2022)

When there is a certain amount of field inhomogeneity, the biased ferrimagnetic crystal can exhibit the higher-order magnetostatic (HMS) mode in addition to the uniform-precession Kittel mode. In cavity magnonics, we show the nonlinearity and heating-induced frequency shifts of the Kittel mode and HMS mode in a yttrium–iron–garnet (YIG) sphere. When the Kittel mode is driven to generate a certain number of excitations, the temperature of the whole YIG sample rises and the HMS mode can display an induced frequency shift, and *vice versa*. This cross effect provides a new method to study the magnetization dynamics and paves a way for novel cavity magnonic devices by including the heating effect as an operational degree of freedom.

Keywords: magnon, magnetostatic mode, temperature, yttrium–iron–garnet (YIG)

PACS: 76.50.+g, 75.30.Gw, 85.70.Ge, 75.10.Hk **DOI:** 10.1088/1674-1056/ac9b02

1. Introduction

Nonlinear effects are a large class of physical phenomena that have been continuously and actively explored in optics,[1–3] plasmonics,[4–6] and acoustics,[7–9] as well as in other oscillations and wave systems.[10–12] Nonlinearity and nonlinear interactions are weak and difficult to be detected in some systems, but they can also become sufficiently strong to be the dominant factor in some other systems. A nonlinear system serves as the basis for further development of applications, such as information processing,[13,14] information conversion,[15] switching devices,[16] and so on.

Cavity magnonics, on the other hand, has gradually demonstrated its unique advantages in fundamental and applied research over the last few years.[17–42] It is expected to be a critical component of hybrid quantum systems[43] and quantum network nodes.[44] A commonly used cavity magnonic system consists of a microwave cavity and ferrimagnets, such as the yttrium–iron–garnet (YIG). The spin collective excitation modes are spin waves in the ferrimagnetic spin ensemble. The most widely studied spin wave mode is the uniform precession mode of spins (*i.e.*, the Kittel mode), which has the largest magnetic dipole moment and can strongly interact with the microwave in both the quantum limit[17,18] and room-temperature classical regime.[19] Under the bias of an external magnetic field with certain inhomogeneity, besides the Kittel mode, there are also higher-order magnetostatic (HMS) modes in the spin ensemble.[45–47] Previous studies often ignored the influence of these magnetostatic modes on the observation and application of Kittel mode in experiments. However, the HMS modes actually have nontrivial spin textures. Their non-zero orbital angular momentum feature can be used to demonstrate nonreciprocal Brillouin light scattering in optomagnonics and other chiral optics.[33,48–50]

In this work, we focus on the heating-induced cross effect on frequency shifts of the Kittel and HMS modes in a nonlinear cavity magnonic system, where the non-linearity is embodied in the self-Kerr effect of magnon mode under strong drive. The heating effect is investigated experimentally in a coupled three-dimensional (3D) cavity and YIG sphere system, where the YIG sphere supports both the Kittel and HMS modes. A large frequency difference between these two modes is found. When the Kittel mode or HMS mode is pumped to generate a certain number of magnon excitations, the pumped mode gains a frequency shift due to the self-Kerr effect.[31,51–56] Meanwhile, the frequency of the undriven mode also shifts due to the driving induced raise of the temperature in the sample. This offers additional controllable degrees of freedom in cavity magnonics without increasing system's complexity. Our study will also bring new ideas to the magnetostatics studies and hybrid magnonic operations.[57–59]

2. System and theoretical model

The experimental setup of the cavity magnonic system is illustrated in Fig. 1(a). It consists of the microwave field in a 3D copper cavity (internal dimension is 44.0 mm × 20.0 mm × 6.0 mm), the magnon modes in a single crystal YIG sphere (1 mm in diameter), and the drive field provided by a microwave (MW) source. The YIG sphere is glued on the top of a beryllium ceramic rod and mounted at the antinode of the magnetic field of the cavity mode TE_{102} ($\omega_c/2\pi = 10.07$ GHz).

†Corresponding author. E-mail: daxu@zju.edu.cn
‡Corresponding author. E-mail: yipuwang@zju.edu.cn

© 2022 Chinese Physical Society and IOP Publishing Ltd

The whole sample is placed in a bias magnetic field B_0 applied along the [110] crystal axis of YIG sphere, which results in a negative self-Kerr coefficient (when the magnon mode is driven, the self-Kerr effect with negative coefficient corresponds to a redshift of the magnon mode frequency).[31,56] The cavity has three ports. The port 1 and port 2 are connected with the vector network analyzer (VNA) for measuring the microwave transmission spectrum $|S_{21}|^2$. The drive field is loaded to port 3, which is terminated with a magnetic coil. The bias magnetic field, the rf magnetic field from the magnetic coil, and the rf magnetic field from the cavity mode TE_{102} are perpendicular to each other at the position of the YIG sphere. This configuration maximizes the cavity–YIG coupling strength and drive efficiency. It should be noted that the rf magnetic field from the cavity is employed as the probing field, which has a far lower intensity than the drive field (rf magnetic field from the magnetic coil). The magnetic coil plays multiple roles: (i) it radiates the drive field; (ii) it works as a dissipative channel for the magnon modes.

More spin moments contribute to the Kittel mode in the crystal, resulting in a larger magnetic dipole and a stronger coupling with the cavity mode.[43,60] Both the Kittel mode and HMS mode become nonlinear modes on account of the magnetocrystalline anisotropy. The magnetocrystalline anisotropy energy measures the energy cost when tuning the magnetization orientation from the easy axis to the hard axis. These energy terms [see Eq. (A4) in Appendix A] give rise to the self-Kerr effect and excitation number bistability.[52] The magnon mode is pumped to generate a certain number of excitations, which increases macrospin precession angle and YIG sphere's temperature due to spin-lattice relaxation, as shown in Fig. 1(b). The temperature alters the magnetocrystalline anisotropy energy and saturation magnetization, which makes all the magnon modes shift in frequency. In previous studies, the cross effect between the Kittel mode and HMS mode has rarely been investigated. Here, we model the two magnon modes with two sub-magnetizations M_K and M_H, where subscripts K and H represent the Kittel mode and HMS mode, respectively. The effective Hamiltonian of the coupled system can be written as (see Appendix B)

$$\begin{aligned} H/\hbar =\ & \omega_c a^\dagger a + (\omega_k + 2K(T))\, b^\dagger b + (\omega_h + 2H(T))\, c^\dagger c \\ & + g_k \left(a^\dagger b + b^\dagger a\right) + g_h \left(a^\dagger c + a c^\dagger\right) \\ & + \Omega_k \left(b^\dagger \mathrm{e}^{-\mathrm{i}\omega_{d1} t} + b\, \mathrm{e}^{\mathrm{i}\omega_{d1} t}\right) \\ & + \Omega_h \left(c^\dagger \mathrm{e}^{-\mathrm{i}\omega_{d2} t} + c\, \mathrm{e}^{\mathrm{i}\omega_{d2} t}\right), \end{aligned} \tag{1}$$

where $a^\dagger$ (a), $b^\dagger$ (b), and $c^\dagger$ (c) are the creation (annihilation) operators of the cavity mode at frequency ω_c, the Kittel mode at frequency ω_k, and the HMS mode at frequency ω_h, respectively; T is the temperature of the sample, which is a function of the excitation number of the magnon mode; $2K(T) = 2K_k(T)(S_K(T) - \langle b^\dagger b\rangle)$ [see Eq. (A5)] and $2H(T) = 2K_h(T)(S_H(T) - \langle c^\dagger c\rangle)$ [see Eq. (B1)] are frequency shifts of the Kittel mode and HMS mode; K_k and K_h are the self-Kerr coefficients of the Kittel mode and HMS mode, respectively; g_k (g_h) is the coupling strength between the Kittel (HMS) mode and cavity mode; Ω_k (Ω_h) is the drive-field strength on the Kittel (HMS) mode, and ω_{d1} (ω_{d2}) is the drive field frequency. It should be noted that we apply only one drive field in the experiment.

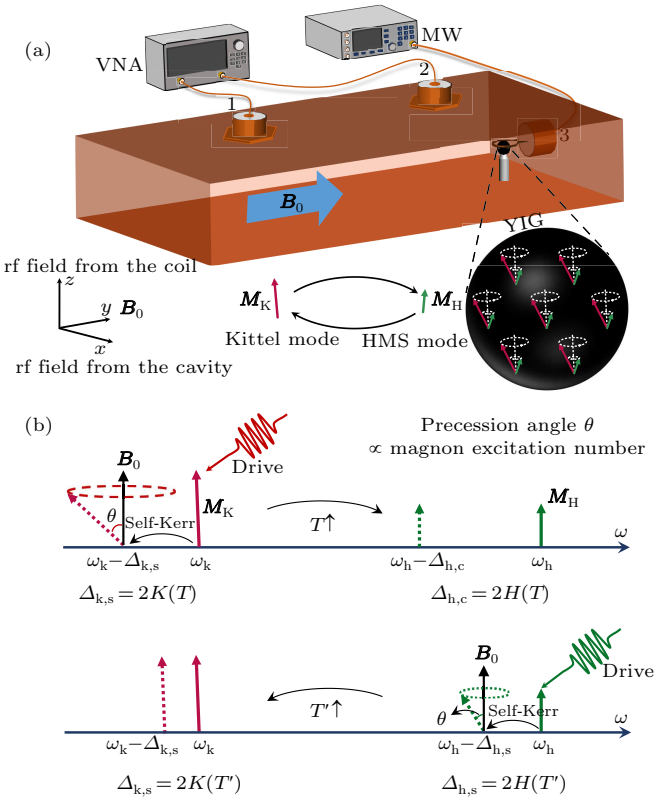


Fig. 1. (a) Schematic diagram of the experimental setup. The YIG sphere is coupled to the cavity mode TE_{102}. The cavity is placed in the bias magnetic field B_0 (blue arrow). The microwave source connected to the loop coil provides a drive field. The vector network analyzer (VNA) measures the cavity transmission spectrum $|S_{21}|^2$. Inset: in the YIG sphere, the Kittel mode and HMS mode are denoted by two sub-magnetizations. (b) Schematic diagram of the self-Kerr and heating effects. In the upper panel, the drive field applied on the Kittel mode excites a certain number of magnons, resulting in an increase of the precession angle θ. The magnon mode dissipates energy into the crystal lattice via spin-lattice relaxation. Then, as the sample is heated and the temperature rises, the self-Kerr effect will shift the frequency of the Kittel mode. The heating effect will shift the frequency of the HMS mode without changing the precession angle of the HMS-mode magnetization M_H. A similar effect occurs by exchanging the roles of the two modes, as shown in the lower panel. The dotted arrows represent the states after driving.

When the drive field is applied nearly resonant to the Kittel mode, $\langle b^\dagger b\rangle \gg \langle c^\dagger c\rangle$ and the temperature rises, as depicted in the top panel of Fig. 1(b). Then, both of the Kittel and HMS modes have frequency shifts. In this case, the frequency shift of the HMS mode is proportional to the excitation number of the Kittel mode, and the precession angle (excitation number) of the HMS mode remains unchanged. This is the mechanism of the heating-induced cross effect on the frequency shift, and

$\Delta_{h,c} = 2H(T)$. Here, the subscript c indicates the cross effect. A similar mechanism occurs when the drive field is applied solely on the HMS mode, as shown in the bottom panel of Fig. 1(b).

3. Experimental results

The transmission spectra of the coupled system are measured *versus* the magnet coil current as shown in Fig. 2(a). The anti-crossing indicates the strong coherent coupling between the Kittel mode and cavity mode, and they will periodically exchange energy with each other.[19] At the left part of the transmission mapping, when the magnet coil current is about 4.75 A, we find a small coupling feature, which is attributed to the HMS mode. The coupling strength is 2 MHz. Here, the frequency difference between the Kittel mode and HMS mode is 301 MHz, which is much lager than the linewidths of the modes. When the magnon mode is pumped by the drive field, the temperature of the sample rises, and be measured by attaching a thermocouple to the surface of the sample.

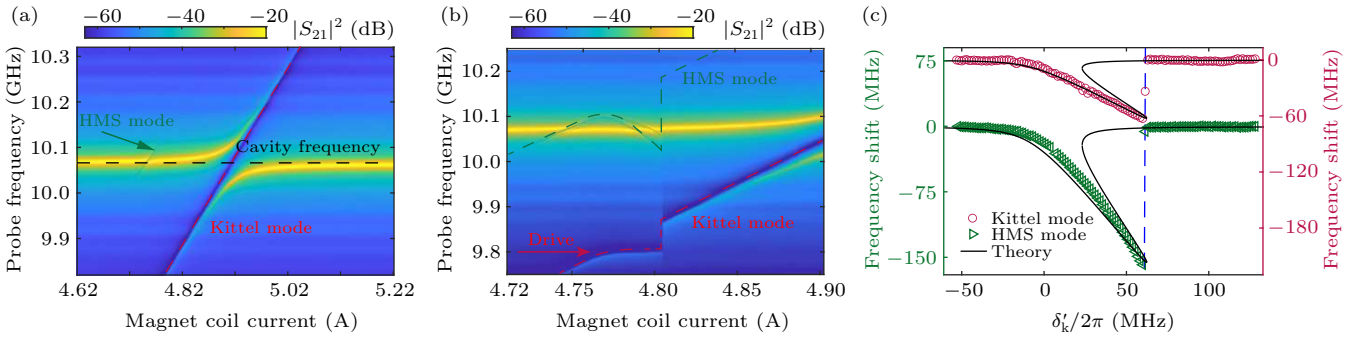


Fig. 2. Drive on the Kittel mode. (a) The transmission spectra are measured *versus* magnet coil current. The Kittel mode (red dashed line) and HMS mode (green dashed line) are coupled with the cavity mode. (b) The transmission spectra are measured *versus* magnet coil current, while a drive field of 9.8 GHz and 25 dBm is applied on the Kittel mode. The Kittel mode has a frequency shift $\Delta_{k,s}$ due to the self-Kerr effect, and the HMS mode has a even larger frequency shift $\Delta_{h,c}$ caused by the heating effect. (c) The frequency shifts of the Kittel mode and HMS mode are extracted from panel (b), and plotted *versus* $\delta_k' = \omega_k - \omega_{d1} - 2\pi \cdot 5.94$ MHz. The experimental results are fitted with Eq. (2) and $\Delta_{h,c} = 2.5\Delta_{k,s}$.

3.1. Drive the Kittel mode

In Fig. 2(b), we apply the drive field with an input power of 25 dBm at the fixed frequency $\omega_{d1}/2\pi = 9.8$ GHz on the Kittel mode and measure the transmission spectra *versus* the magnetic coil current. Typical bistable frequency jumps can be observed in both the Kittel mode and HMS mode. This measurement is equivalent to sweeping the frequency of the drive field while fixing the frequencies of the magnon modes. We define the drive-field detuning as $\delta_k = \omega_k - \omega_{d1}$. It should be noted that our system works in the double-dispersive regime, where $\Lambda_{c,k} = \omega_c - \omega_k \gg g_k$ and $\Lambda_{h,k} = \omega_h - \omega_k \gg g_h$. The coherent couplings induced-frequency shifts are approximately equal to $g_k^2/\Lambda_{c,k}$ and $g_h^2/\Lambda_{h,k}$, respectively.[51,52] In the dispersive regime, they are all small terms. Also, the coupling strength between the HMS mode and cavity mode is relatively small. In this case, we can intently pay attention to the effects induced by Kerr nonlinearity. Then we extract and plot the frequency shifts of the two magnon modes *versus* $\delta_k'/2\pi = \delta_k/2\pi - 5.94$ MHz in Fig. 2(c). The driven Kittel mode has a maximum frequency shift of about -60 MHz, and the undriven HMS mode has a synchronous frequency shift of about -150 MHz. In this case, the temperature of the YIG sphere rises from approximately 300 K to 360 K. The temperature increasement of the YIG sphere results from the spin-lattice relaxation process. The magnons pumped by the drive field dissipate their energy to the lattice vibration phonon mode.

The frequency shift $\Delta_{k,s}$ of the driven Kittel mode can be fitted by the following equation[51,52] [see Eq. (B7)]:

$$\left[\left(\Delta_{k,s} + \delta_k'\right)^2 + \gamma_k'^2\right]\Delta_{k,s} - c_k P_{d1} = 0, \tag{2}$$

where $\delta_k' = \delta_k - \eta\delta_c$ and $\gamma_k' = \gamma_k/2 + \eta\kappa_c/2$ with $\eta = g_k^2/\left(\delta_c^2 + \kappa_c^2/4\right)$ are the effective drive-field detuning and the effective damping rate of the Kittel mode, respectively. $g_k/2\pi = 40.5$ MHz is the coupling strength between the Kittle mode and the cavity mode. $\delta_c/2\pi = \omega_c/2\pi - \omega_{d1}/2\pi = 270$ MHz is the frequency difference between the cavity mode and the drive field. $\kappa_c/2\pi = 3.1$ MHz and $\gamma_k/2\pi = 11.6$ MHz are the cavity mode linewidth and the Kittle mode linewidth, respectively. Therefore, $\eta = 0.022$ and $\delta_k'/2\pi = \delta_k/2\pi - 5.94$ MHz. c_k is a parameter reflecting the drive efficiency of the drive field, and P_{d1} is the drive power. The fitting curves are shown as solid black lines in Fig. 2(c), which are in good agreement with the experimental results. We get the ratio of $H(360\text{ K})/K(360\text{ K})$ equals 2.5.

3.2. Drive the HMS mode

The cross effect on the frequency shift implies that the HMS mode excitation will also induce a frequency shift of the Kittel mode. Next, we apply the drive field (25 dBm) at a fixed frequency $\omega_{d2}/2\pi = 10.1$ GHz on the HMS mode and sweep the magnetic field. The measured transmission mapping is shown in Fig. 3(a). As expected, the HMS mode has a

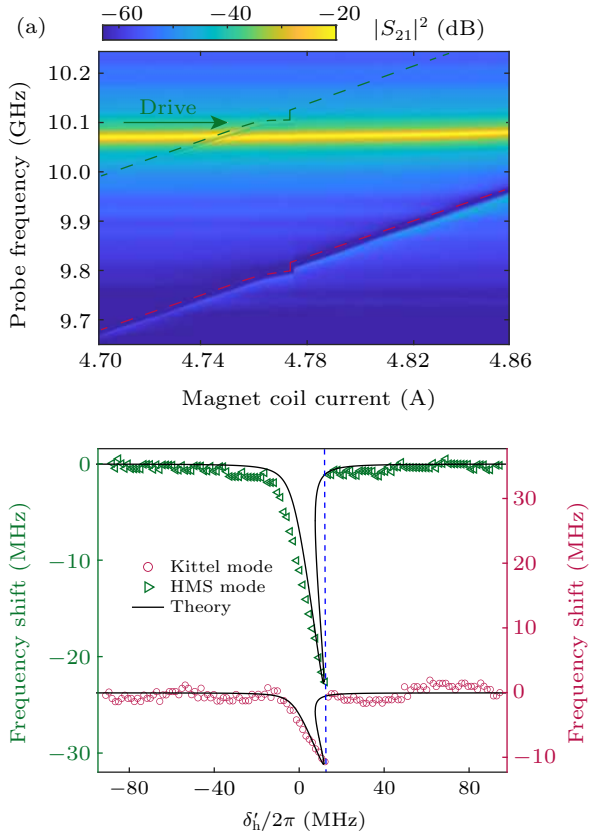


Fig. 3. Drive on the HMS mode. (a) The transmission spectra are measured *versus* magnet coil current, while a drive field of 10.1 GHz and 25 dBm is applied on the HMS mode. The HMS mode has a frequency shift $\Delta_{h,s}$ due to the self-Kerr effect, and the Kittel mode has a smaller frequency shift $\Delta_{k,c}$ caused by the heating effect. (b) The frequency shifts of the Kittel mode and HMS mode are extracted from panel (a), and plotted *versus* δ_h'. The experimental results are fitted using Eq. (3) and $\Delta_{k,c} = 2.1\Delta_{h,s}$.

frequency shift due to the self-Kerr effect, and simultaneously the heating-induced cross effect shifts the frequency of the Kittel mode. We extract the frequency shifts of these two modes *versus* the effective drive-field detuning δ_h' as shown in Fig. 3(b). In this case, the temperature of the YIG sphere is increased from 300 K to about 310 K. Similarly, the self-Kerr effect induced frequency shift $\Delta_{h,s}$ of the HMS mode obeys the following equation:

$$\left[\left(\Delta_{h,s}+\delta_h'\right)^2+\gamma_h'^2\right]\Delta_{h,s}-c_h P_{d2}=0, \tag{3}$$

where $\delta_h' = \delta_h - \eta\delta_c$ and $\gamma_h' = \gamma_h/2 + \eta\kappa_c/2$ with $\eta = g_h^2/\left(\delta_c^2+\kappa_c^2/4\right)$ are the effective drive-field detuning and the effective damping rate of the HMS mode, respectively. $g_h/2\pi = 2$ MHz is the coupling strength between the HMS mode and the cavity mode. $\delta_c/2\pi = \omega_c/2\pi - \omega_{d2}/2\pi = 30$ MHz is the frequency difference between the cavity mode and the drive field. $\gamma_h/2\pi = 5$ MHz is the HMS mode linewidth. Therefore, $\eta = 0.004$ and $\delta_h' \approx \delta_h$. c_h is the parameter reflecting the drive efficiency of the drive field on the HMS mode. The fitting curves are shown as black lines in Fig. 3(b). We get $H(310\text{ K})/K(310\text{ K}) = 2.1$. It should be noted that the temperature increasement in the Kittel mode-driven case is greater than that in the HMS mode-driven case because the dipole moment of the HMS mode is substantially smaller than that of the Kittel mode.

4. Conclusion

In this work, we investigated the heating-induced cross-frequency shifts when the magnon mode is pumped in a ferrimagnetic spin ensemble, in which one Kittel mode and one higher-order magnetostatic mode co-exist. The heating-incuced cross effect between them plus their individual self-Kerr effects gives rise to fascinating phenomena. In the experiment, we drive the Kittel mode and the higher-order magnetostatic mode, respectively. Our experiment opens up a new path to study nonlinear effects in magnetic materials and spin ensembles. The mutual interaction between different magnetostatic modes in a single YIG sample can also provide new degrees of freedom for cavity spintronics and cavity magnonics.[61] We anticipate that this finding may stimulate more designs and applications of cavity magnonics.

Acknowledgments

Project supported by the National Natural Science Foundation of China (Grants Nos. 11934010, U1801661, and 12174329), the Zhejiang Province Program for Science and Technology (Grant No. 2020C01019), the Fundamental Research Funds for the Central Universities (Grant No. 2021FZZX001-02), and the China Postdoctoral Science Foundation (Grant No. 2019M660137).

Appendix A: Hamiltonian of the kittel mode

First, we derive the Hamiltonian of the magnon modes without including the heating effect. Under the bias magnetic field B_0, the Hamiltonian of the Kittel mode is written as (HMS mode has a similar form)[51]

$$H_k = -\int_V \boldsymbol{M}_K\cdot\boldsymbol{B}_0\,\mathrm{d}\tau - \frac{\mu_0}{2}\int_V \boldsymbol{M}_K\cdot\boldsymbol{H}_{an}\,\mathrm{d}\tau, \tag{A1}$$

where the first term represents the Zeeman energy and the second term is the magnetocrystalline anisotropy energy, $\boldsymbol{M}_K = (M_{K,x}, M_{K,y}, M_{K,z})$ is the sub-magnetization corresponding to the Kittel mode, V is the volume of the YIG sphere, μ_0 is the vacuum permeability, and $\boldsymbol{H}_{an}$ is the anisotropic field due to the magnetocrystalline anisotropy in the YIG crystal.

We adopt the direction of the bias magnetic $\boldsymbol{B}_0$ as the z direction ($\boldsymbol{B}_0 = B_0\boldsymbol{e}_z$). When the [110] crystal axis of the YIG sphere is aligned along the bias magnetic field, the anisotropic

field is given by[62]

$$\boldsymbol{H}_{\rm an} = \frac{3K_{\rm an}M_x}{\mu_0 M^2}\boldsymbol{e}_x + \frac{9K_{\rm an}M_y}{4\mu_0 M^2}\boldsymbol{e}_y + \frac{K_{\rm an}M_z}{\mu_0 M^2}\boldsymbol{e}_z, \tag{A2}$$

where $K_{\rm an}$ is the first-order magnetocrystalline anisotropy constant. Then, the Hamiltonian of the Kittel mode has the form

$$\begin{aligned} H_{\rm k} = & -B_0 M_{{\rm K},z}V - \frac{3K_{\rm an}M_{{\rm K},x}}{2M_{\rm K}^2}\boldsymbol{e}_x \\ & - \frac{9K_{\rm an}M_{{\rm K},y}}{8M_{\rm K}^2}\boldsymbol{e}_y - \frac{K_{\rm an}M_{{\rm K},z}}{2M_{\rm K}^2}\boldsymbol{e}_z. \end{aligned} \tag{A3}$$

By using the macrospin operator $\boldsymbol{S} = \boldsymbol{M}V/\hbar\gamma \equiv (S_x, S_y, S_z)$, where γ is the electronic gyromagnetic ratio,[63] the Hamiltonian $H_{\rm k}$ can be written as

$$\begin{aligned} H_{\rm k}/\hbar = & -\gamma B_0 S_{{\rm K},z} - \frac{3\hbar K_{\rm an}\gamma^2}{2M_{\rm K}^2 V}S_{{\rm K},x}^2 \\ & - \frac{9\hbar K_{\rm an}\gamma^2}{8M_{\rm K}^2 V}S_{{\rm K},y}^2 - \frac{\hbar K_{\rm an}\gamma^2}{2M_{\rm K}^2 V}S_{{\rm K},z}^2. \end{aligned} \tag{A4}$$

We harness the Holstein–Primakoff transformation:[64] $S_{\rm K}^+ = \sqrt{2S_{\rm K} - b^\dagger b}\,b$, $S_{\rm K}^- = b^\dagger\sqrt{2S_{\rm K} - b^\dagger b}$, and $S_{{\rm K},z} = S_{\rm K} - b^\dagger b$, where $S_{\rm K}$ is the total spin number, and $S_{\rm K}^\pm = S_{{\rm K},x} \pm {\rm i}S_{{\rm K},y}$. The excited magnon number is small compared with the total spin number $S_{\rm K}$, and the higher-order terms can be neglected in the Holstein–Primakoff transformation. Under the rotating-wave and mean-field approximation, we finally obtain the Hamiltonian for the Kittel mode

$$\begin{aligned} H_{\rm k}/\hbar &= (\gamma B_0 + 2K_{\rm k}(T)S_{\rm K}(T))b^\dagger b - K_{\rm k}(T)b^\dagger b b^\dagger b \\ &= \left[\gamma B_0 + 2K_{\rm k}(T)\left(S_{\rm K}(T) - \left\langle b^\dagger b\right\rangle\right)\right]b^\dagger b \\ &= (\omega_{\rm k} + 2K(T))b^\dagger b, \end{aligned} \tag{A5}$$

where $\omega_{\rm k} = \gamma B_0$, and $K(T) = K_{\rm k}(T)(S_{\rm K}(T) - \langle b^\dagger b\rangle)$. Because the magnon mode dissipates its energy to the lattice via spin-lattice relaxation,[65] the temperature of the sample is a function of the excitation number, *i.e.*, $T = T(\langle b^\dagger b\rangle)$. Here, $K_{\rm k}$ represents the self-Kerr coefficient of the Kittel mode. From Eqs. (A4) and (A5), we can get

$$K_{\rm k}(T) = -13\hbar K_{\rm an}(T)\gamma^2/(16VM_{\rm K}^2(T)), \tag{A6}$$

which is a function of temperature because both $K_{\rm an}$ and $M_{\rm K}$ are temperature-dependent.[66,67]

Appendix B: Heating-induced cross effect on the frequency shifts

The first-order magnetocrystalline anisotropy constant $K_{\rm an}$, saturation magnetization $M_{\rm K}$, and $S_{\rm K}$ are all temperature-dependent. Consequently, temperature change can alter the Kerr coefficient and the magnon mode frequency. To quantify the impact of temperature on the frequency shift, we measured the temperature dependence of magnon mode frequency from approximately 300 K to 350 K, as shown in Fig. B1. It can be seen that the ferromagnetic resonance (FMR) frequency of the sample varies with temperature, but there is no bistability during the external heating and cooling.

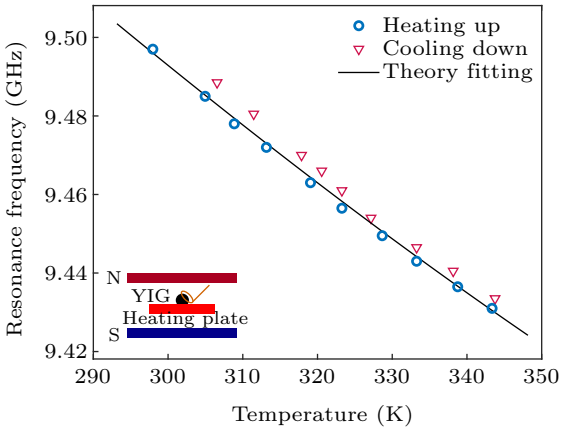


Fig. B1. Magnon mode frequency–temperature dependence. The YIG sphere is placed on a heating plate, and a digital controller regulates the temperature of the entire plate accurately with auto tuning function. The resonant frequency of the magnon mode in the fixed bias magnetic field is measured by a loop antenna, as shown in the inset figure. In this temperature range, an approximately linear relationship is obtained.

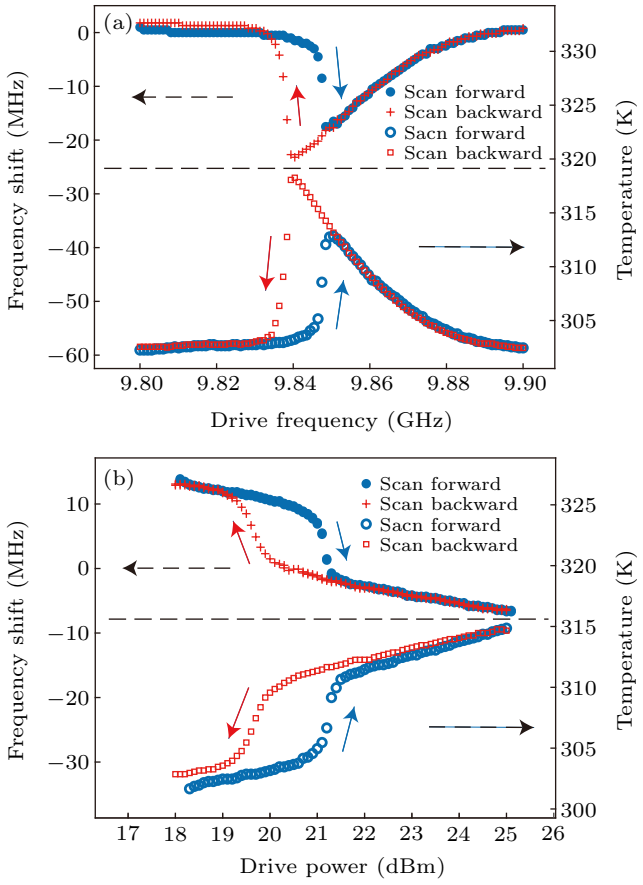


Fig. B2. (a) The temperature (bottom panel) of the sample and the magnon mode frequency shift (top panel) *versus* drive frequency. The drive power is fixed at 25 dBm. (b) The temperature (bottom panel) of the sample and the magnon mode frequency shift (top panel) *versus* drive power. The drive frequency is $\omega_{\rm d}/2\pi = 9.86$ GHz.

While sweeping the drive frequency or drive power, we simultaneously monitor the frequency shift of the magnon mode and the sample's temperature. The experimental results are displayed in Fig. B2. We can find that both the magnon mode frequency shift and temperature exhibit bistable behaviors. In our setup, the drive power required for obtaining magnon mode frequency shift is relatively large, but it can be reduced by utilizing a planar waveguide structure.[69] In fact, it is the bistability of the magnon excitation number that causes the simultaneous temperature bistability. Then, the temperature shifts the magnon frequency. The same holds for the refractive index of the YIG sample, where the thermal bistability is observed by measuring the optical resonance signal.[68] When one of the magnon modes in the sphere is excited, the temperature of the entire sample rises, which changes the saturation magnetization and magnetocrystalline anisotropy field of the sphere. The temperature change further affects the frequencies of other magnon modes in the sphere. Subsequently, the total Hamiltonian can be written as

$$\begin{aligned} H/\hbar =\ & \omega_{\rm c} a^{\dagger}a + (\omega_{\rm k}+2K(T))\, b^{\dagger}b + (\omega_{\rm h}+2H(T))\, c^{\dagger}c \\ & + g_{\rm k}\left(a^{\dagger}b + b^{\dagger}a\right) + g_{\rm h}\left(a^{\dagger}c + ac^{\dagger}\right) \\ & + \Omega_{\rm k}\left(b^{\dagger}\,{\rm e}^{-{\rm i}\,\omega_{\rm d1}t} + b\,{\rm e}^{{\rm i}\,\omega_{\rm d1}t}\right) \\ & + \Omega_{\rm h}\left(c^{\dagger}\,{\rm e}^{-{\rm i}\,\omega_{\rm d2}t} + c\,{\rm e}^{{\rm i}\,\omega_{\rm d2}t}\right), \end{aligned} \tag{B1}$$

in the above equation, the effective Kerr coefficients $K(T) = K_{\rm k}(T)\left(S_{\rm K}(T) - \langle b^{\dagger}b\rangle\right)$, and $H(T) = K_{\rm h}(T)(S_{\rm H}(T) - \langle c^{\dagger}c\rangle)$, which are functions of the sample's temperature and the excitation number of mangon. With the Hamiltonian in Eq. (B1), we can obtain the quantum Langevin equations for the cavity magnonic system in the case of driving the Kittel mode[52]

$$\begin{aligned} \frac{{\rm d}a}{{\rm d}t} &= -{\rm i}\left(\delta_{\rm c} - {\rm i}\frac{\kappa_{\rm c}}{2}\right)a - {\rm i}g_{\rm k}b, \\ \frac{{\rm d}b}{{\rm d}t} &= -{\rm i}\left(\delta_{\rm k} + \Delta_{\rm k,s} - {\rm i}\frac{\gamma_{\rm k}}{2}\right)b - {\rm i}g_{\rm k}a - {\rm i}\Omega_{\rm k}, \end{aligned} \tag{B2}$$

where $\delta_{\rm c(k)} = \omega_{\rm c(k)} - \omega_{\rm d1}$, $\kappa_{\rm c}$ is the total damping rate of the cavity mode, $\gamma_{\rm k}$ is the damping rate of the Kittel mode, and $\Delta_{\rm k,s} = 2K(T)$ is the frequency shift of the Kittel mode. Then we rewrite the operator as a sum of the steady-state value and the fluctuation, *i.e.*, $a = A + \delta a$ and $b = B + \delta b$. It follows from Eq. (B2) that A and B satisfy

$$\begin{aligned} \frac{{\rm d}A}{{\rm d}t} &= -{\rm i}\left(\delta_{\rm c} - {\rm i}\frac{\kappa_{\rm c}}{2}\right)A - {\rm i}g_{\rm k}B, \\ \frac{{\rm d}B}{{\rm d}t} &= -{\rm i}\left(\delta_{\rm k} + \Delta_{\rm k,s} - {\rm i}\frac{\gamma_{\rm k}}{2}\right)B - {\rm i}g_{\rm k}A - {\rm i}\Omega_{\rm k}. \end{aligned} \tag{B3}$$

When the system reaches steady state, we have ${\rm d}A/{\rm d}t = 0$ and ${\rm d}B/{\rm d}t = 0$. From Eq. (B3), we obtain

$$\left(\delta_{\rm c} - {\rm i}\frac{\kappa_{\rm c}}{2}\right)A + g_{\rm k}B = 0,$$

$$\left(\delta_{\rm k} + \Delta_{\rm k,s} - {\rm i}\frac{\gamma_{\rm k}}{2}\right)B + g_{\rm k}A + \Omega_{\rm k} = 0. \tag{B4}$$

Eliminating A in Eq. (B4), we get

$$\left(\delta'_{\rm k} + \Delta_{\rm k,s} - {\rm i}\gamma'_{\rm k}\right)B + \Omega_{\rm k} = 0, \tag{B5}$$

where $\delta'_{\rm k} = \delta_{\rm k} - \eta\delta_{\rm c}$, $\gamma'_{\rm k} = \gamma_{\rm k}/2 + \eta\kappa_{\rm c}/2$, and $\eta = g_{\rm k}^2/\left(\delta_{\rm c}^2 + \kappa_{\rm c}^2/4\right)$. Using Eq. (B5) and its complex conjugate expression, we obtain

$$\left[\left(\delta'_{\rm k} + \Delta_{\rm k,s}\right)^2 + \gamma_{\rm k}'^2\right]|B|^2 - cP_{\rm d1} = 0, \tag{B6}$$

where $P_{\rm d1}$ is the drive power and c is a constant coefficient reflecting the drive efficiency of the drive field. It should be noted that the frequency shift of the magnon mode is proportional to $|B|^2$. Then, we replace $|B|^2$ in Eq. (B6) with $\Delta_{\rm k,s}$. Meanwhile, an additional factor could be incorporated into $c_{\rm k}$, *i.e.*, $c_{\rm k} = c(\Delta_{\rm k,s}/|B|^2)$. Finally, we obtain

$$\left[\left(\delta'_{\rm k} + \Delta_{\rm k,s}\right)^2 + \gamma_{\rm k}'^2\right]\Delta_{\rm k,s} - c_{\rm k}P_{\rm d1} = 0. \tag{B7}$$

Similarly, we can obtain the equation of the frequency shift of the HMS mode when the drive field is applied on the HMS mode. It reads

$$\left[\left(\delta'_{\rm h} + \Delta_{\rm h,s}\right)^2 + \gamma_{\rm h}'^2\right]\Delta_{\rm h,s} - c_{\rm h}P_{\rm d2} = 0, \tag{B8}$$

where $\delta'_{\rm h} = \delta_{\rm h} - \eta\delta_{\rm c}$, $\gamma'_{\rm h} = \gamma_{\rm h}/2 + \eta\kappa_{\rm c}/2$, and $\eta = g_{\rm h}^2/\left(\delta_{\rm c}^2 + \kappa_{\rm c}^2/4\right)$.

Appendix C: Data processing method

The transmission spectrum mapping consists of transmission spectra measured at different bias magnetic fields, as shown in Fig. C1(a). The individual transmission spectrum is depicted in Fig. C1(b). The anti-resonances correspond to various modes; for example, the green triangle dot represents the HMS mode, and the circle red dot denotes the Kittel mode. We extract the data points from the transmission spectra and plot them in the left panel of Fig. C1(c). We convert coordinates to frequency shift *versus* driving detuning due to its convenience for us to fit. First, we subtract the linear component that increases with the external bias field from all data points. The remaining component is the contribution of frequency shift caused by the driving field. Second, converting bias current to linear frequency. Third, we replace the horizontal axis with drive detuning $\delta'_{\rm k} = \omega_{\rm k} - \omega_{\rm d1} - 2\pi\cdot 5.94$ MHz and fit it using Eq. (2).

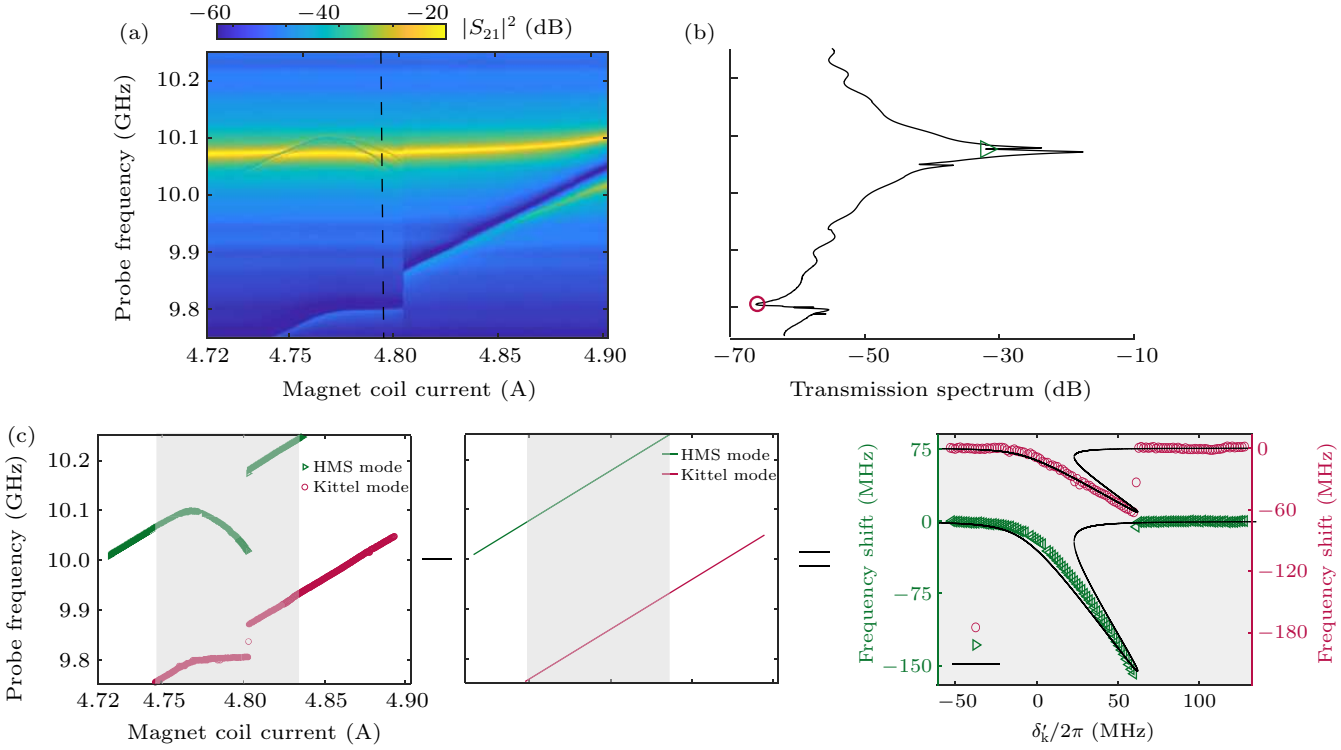


Fig. C1. (a) Original transmission spectrum mapping. (b) The transmission spectrum $|S_{21}|^2$ corresponds to the black dashed line labelled in (a) at a certain bias magnetic field. (c) The Kerr effect induced frequency shifts are extracted. We subtract the linear frequency shift caused by the external bias field from all data points. The horizontal axis is changed to $\delta'_k = \omega_k - \omega_{d1} - 2\pi \cdot 5.94$ MHz when fitting with Eq. (2).

References

[1] Boyd R W 2020 *Nonlinear Optics* (London: Academic Press)

[2] Auere A, Jussila H, Dai Y, Wang Y, Lipsanen H and Sun Z 2018 *Adv. Mater.* **30** 1705963

[3] Zhang X, Cao Q T, Wang Z, Liu Y, Qiu C W, Yang L, Gong Q and Xiao Y F 2019 *Nat. Photon.* **13** 21

[4] Kauranen M and Zayats A V 2012 *Nat. Photon.* **6** 737

[5] Mesch M, Metzger B, Hentschel M and Giessen H 2016 *Nano Lett.* **16** 3155

[6] Zhong J H, Vogelsang J, Yi J M, Wang D, Wittenbecher L, Mikaelsson S, Korte A, Chimeh A, Arnold C L, Schaaf P, Runge E, Huillier A L, Mikkelsen A and Lienau C 2020 *Nat. Commun.* **11** 1464

[7] Hamilton M F, Blackstock D T and Ostrovsky L A 1999 *J. Acoust. Soc. Am.* **105** 578

[8] Fang X, Wen J, Bonello B, Yin J and Yu D 2017 *Nat. Commun.* **8** 1288

[9] Darabi A, Fang L, Mojahed A, Fronk M D, Vakakis A F and Leamy M J 2019 *Phys. Rev. B* **99** 214305

[10] Nayfeh A H and Mook D T 2008 *Nonlinear Oscillations* (New York: John Wiley & Sons)

[11] Kartashov Y V, Astrakharchik G E, Malomed B A and Torner L 2019 *Nat. Rev. Phys.* **1** 185

[12] Zuo Y, Yu W, Liu C, Cheng X, Qiao R, Liang J, Zhou X, Wang J, Wu M, Zhao Y, Gao P, Wu S W, Sun Z P, Liu K H, Bai X D and Liu Z F 2020 *Nat. Nanotechnol.* **15** 987

[13] Bergeal N, Vijay R, Manucharyan V E, Siddiqi I, Schoelkopf R J, Girvin S M and Devoret M H 2010 *Nat. Phys.* **6** 296

[14] Wu B J and Gao X 2008 *Chin. Phys. Lett.* **25** 4006

[15] Nozaki K, Matsuo S, Fujii T, Takeda K, Shinya A, Kuramochi E and Notomi M 2019 *Nat. Photon.* **13** 454

[16] Suchkov S V, Sukhorukov A A, Huang J, Dmitriev S V, Lee C and Kivshar Y S 2016 *Laser Photon. Rev.* **10** 177

[17] Huebl H, Zollitsch C W, Lotze J, Hocke F, Greifenstein M, Marx A, Gross R and Goennenwein S T B 2013 *Phys. Rev. Lett.* **111** 127003

[18] Tabuchi Y, Ishino S, Ishikawa T, Yamazaki R, Usami K and Nakamura Y 2014 *Phys. Rev. Lett.* **113** 083603

[19] Zhang X, Zou C L, Jiang L and Tang H X 2014 *Phys. Rev. Lett.* **113** 156401

[20] Goryachev M, Farr W G, Creedon D L, Fan Y, Kostylev M and Tobar M E 2014 *Phys. Rev. Appl.* **2** 054002

[21] Bai L, Harder M, Chen Y P, Fan X, Xiao J Q and Hu C M 2015 *Phys. Rev. Lett.* **114** 227201

[22] Cao Y, Yan P, Huebl H, Goennenwein S T B and Bauer G E W 2015 *Phys. Rev. B* **91** 094423

[23] Zhang X, Zou C L, Zhu N, Marquardt F, Jiang L and Tang H X 2015 *Nat. Commun.* **6** 8914

[24] Tabuchi Y, Ishino S, Noguchi A, Ishikawa T, Yamazaki R, Usami K and Nakamura Y 2015 *Science* **349** 405

[25] Zhang D, Wang X M, Li T F, Luo X Q, Wu W, Nori F and You J Q 2015 *npj Quantum Inform.* **1** 15014

[26] Haigh J A, Nunnenkamp A, Ramsay A J and Ferguson A J 2016 *Phys. Rev. Lett.* **117** 133602

[27] Maier-Flaig H, Harder M, Gross R, Huebl H and Gonnenwein S T B 2016 *Phys. Rev. B* **94** 054433

[28] Osada A, Hisatomi R, Noguchi A, Tabuchi Y, Yamazaki R, Usami K, Sadgrove M, Yalla R, Nomura M and Nakamura Y 2016 *Phys. Rev. Lett.* **116** 223601

[29] Zhang X, Zhu N, Zou C L and Tang H X 2016 *Phys. Rev. Lett.* **117** 123605

[30] Zhang D, Luo X Q, Wang Y P, Li T F and You J Q 2017 *Nat. Commun.* **8** 1368

[31] Wang Y P, Zhang G Q, Zhang D, Li T F, Hu C M and You J Q 2018 *Phys. Rev. Lett.* **120** 057202

[32] Li J, Zhu S Y and Agarwal G S 2018 *Phys. Rev. Lett.* **121** 203601

[33] Osada A, Gloppe A, Hisatomi R, Noguchi A, Yamazaki R, Nomura M, Nakamura Y and Usami K 2018 *Phys. Rev. Lett.* **120** 133602

[34] Harder M, Yang Y, Yao B M, Yu C H, Rao J W, Gui Y S, Stamps R L and Hu C M 2018 *Phys. Rev. Lett.* **121** 137203

[35] Wang Y P, Rao J W, Yang Y, Xu P C, Gui Y S, Yao B M, You J Q, and Hu C M 2019 *Phys. Rev. Lett.* **123** 127202

[36] Lachance-Quirion D, Wolski S P, Tabuchi Y, Kono S, Usami K and Nakamura Y 2020 *Science* **367** 425

[37] Yang Y, Wang Y P, Rao J W, Gui Y S, Yao B M, Lu W and Hu C M 2020 *Phys. Rev. Lett.* **125** 147202

[38] Xu J, Zhong C, Han X, Jin D, Jiang L and Zhang X 2020 *Phys. Rev. Lett.* **125** 237201

[39] Wolski S P, Lachance-Quirion D, Tabuchi Y, Kono S, Noguchi A, Usami K and Nakamura Y 2020 *Phys. Rev. Lett.* **125** 117701

[40] Rao J W, Xu P C, Gui Y S, Wang Y P, Yang Y, Yao B, Dietrich J, Bridges G E, Fan X L, Xue D S and Hu C M 2021 *Nat. Commun.* **12** 1933

[41] Xu J, Zhong C, Han X, Jin D, Jiang L and Zhang X 2021 *Phys. Rev. Lett.* **126** 207202

[42] Potts C A, Varga E, Bittencourt V A S V, Kusminskiy S V and Davis J P 2021 *Phys. Rev. X* **11** 031053

[43] Lachance-Quirion D, Tabuchi Y, Gloppe A, Usami K and Nakamura Y 2019 *Appl. Phys. Express* **12** 070101

[44] Li J, Wang Y P, Wu W J, Zhu S Y and You J Q 2021 *PRX Quantum* **2** 040344

[45] Li S F, He P, Cheng C Y, Zhou S M and Lai T S 2014 *Chin. Phys. Lett.* **31** 017502

[46] Dillon J F and Jr 1958 *Phys. Rev.* **112** 59

[47] Fletcher P C and Bell R O 1959 *J. Appl. Phys.* **30** 687

[48] Graf J, Pfeifer H, Marquardt F and Kusminskiy S V 2018 *Phys. Rev. B* **98** 241406

[49] Haigh J A, Lambert N J, Sharma S, Blanter Y M, Bauer G E W and Ramsay A J 2018 *Phys. Rev. B* **97** 214423

[50] Osada A, Gloppe A, Nakamura Y and Usami K 2018 *New J. Phys.* **20** 103018

[51] Wang Y P, Zhang G Q, Zhang D, Luo X Q, Xiong W, Wang S P, Li T F, Hu C M and You J Q 2016 *Phys. Rev. B* **94** 224410

[52] Zhang G Q, Wang Y P and You J Q 2019 *Sci. China-Phys. Mech. Astron.* **62** 987511

[53] Kong C, Xiong H and Wu Y 2019 *Phys. Rev. Appl.* **12** 034001

[54] Bi M X, Yan X H, Zhang Y and Xiao Y 2021 *Phys. Rev. B* **103** 104411

[55] Shen R C, Wang Y P, Li J, Zhu S Y, Agarwal G S and You J Q 2021 *Phys. Rev. Lett.* **127** 183202

[56] Gurevich A G and Melkov G A 2020 *Magnetization Oscillations and Waves* (Boca Raton: CRC Press)

[57] Li Y, Zhang W, Tyberkevych V, Kwok W K, Hoffmann A and Novosad V 2020 *J. Appl. Phys.* **128** 130902

[58] Rameshti B Z, Kusminskiy S V, Haigh J A, Usami K, Lachance-Quirion D, Nakamura Y, Hu C M, Tang H X, Bauer G E W and Blanter Y M 2022 *Phys. Rep.* **979** 1

[59] Yuan H Y, Cao Y, Kamra A, Duine R A and Yan P 2022 *Phys. Rep.* **965** 1

[60] Zhang C, Jia C, Shi Y, Jiang C, Xue D, Ong C K and Chai G 2021 *Phys. Rev. B* **103** 184427

[61] Chumak A V, Kabos P, Wu M, *et al.* 2021 arXiv: 2111.00365

[62] Prabhakar A and Stancil D D 2009 *Spin waves: Theory and applications* (New York: Springer)

[63] Soykal Ö O and Flatté M E 2010 *Phys. Rev. Lett.* **104** 077202

[64] Holstein T and Primakoff H 1940 *Phys. Rev.* **58** 1098

[65] Sanders D J and Walton D 1977 *Phys. Rev. B* **15** 1489

[66] Hansen P, Röschmann P and Tolksdorf W 1974 *J. Appl. Phys* **45** 2728

[67] Hansen P 1974 *J. Appl. Phys.* **45** 3638

[68] Chai C Z, Hu X X, Zou C L, Guo G C and Dong C H 2019 *Appl. Phys. Lett.* **114** 021101

[69] Lin F Q, Zhang S H, Zhao G X, Li H F, Zong W H and Li S D 2020 *Chin. Phys. B* **29** 067601